FEM Parameterized Sensorless Vector Control of Permanent Magnet Synchronus Machines using High-Frequency Synchronous Voltage Injection Method

Gergely Szabó, Károly Veszprémi

Department of Electric Power Engineering, Faculty of Electrical Engineering and Informatics, Budapest University of Technology and Economics
Műegyetem rkp. 3, H-1111 Budapest, Hungary
szabo.gergely@edu.bme.hu, veszpremi.karoly@vik.bme.hu

Abstract: The authors of the paper present the high-frequency synchronous voltage injections-based sensorless vector control method on an interior permanent magnet synchronous machine (IPMSM). For development and testing purposes a lumped-parameter, saturating machine model was created and will be presented, which also involves cogging torque effects. The presented machine model runs faster than the coupled simulations allowing to develop the control algorithms much faster. The machine model was obtained by combining the finite element method (FEM) analysis's results with the space vector-based equations. The sensorless algorithm will be detailed, followed by the proposed estimator structure. The authors present a new dynamic model for the PLL-based synchronous injection estimator, making possible to tune its PI controller. Parameter sensitivity and stability analysis will be presented, based on the proposed estimator structure and FEM analysis results. Simulation result are presented, compared, and validated by experimental measurement results.

Keywords: Vector Control; Permanent Magnet Synchronous Machine; Sensorless Control; High-Frequency Signal Injection

1 Introduction

The vector control algorithms of AC drives have an important common property; all of them require the common coordinate system's angle. This angle can be obtained using a shaft angle encoder or with a sensorless algorithm. In case of shaft angle encoder, the property and the dynamics of the encoder highly influence the drive control method. The main differences are usually the sensing capabilities of the encoder, meaning whether is it able to provide absolute or relative angle. Another can be the sensing principle of the selected encoder which usually defines

whether the encoder is shaft-mounted or contactless. Nevertheless, the communication interface of the encoder must be taken into account during the selection process.

A sensorless vector control methods try to eliminate, or supplement the speed encoder in the controlled electric drives. The combination of the sensored and sensorless methods can be beneficial in many aspects. First, the system's safety level can be increased, and the sensorless method can be used as a backup algorithm if the physical encoder fails, on the other hand cheaper encoders can be used, and their disadvantageous properties can be compensated with the sensorless method. A good example can be an incremental encoder, which is not able to provide absolute angle information during the initial state of the drive system. This can be compensated with a sensorless method, which is capable finding the initial angle, and also providing accurate results in the low-speed regions.

Among the sensorless methods, the high-frequency injection methods try exploiting the magnetic anisotropies coming from the machine's design. These injection-based solutions can provide good performance in low-frequency regions, where many of the sensorless methods fail [1], [2]. Since most of the controlled electric drives involve a voltage source inverter, therefore voltage injection is an obvious choice. Based on the place of injection rotating and synchronous methods can be distinguished. The first solution adds test signals to the terminal voltages in the stationary reference frame [3] - [5]. The common coordinate system's angle is calculated from the measured current response, using a chain of filters and additional compensation algorithms. The synchronous injection methods add test signals in the estimated common coordinate system [6] - [8], in which coordinate system the signal processing is implemented. This usually involves a low-pass filter (LPF) and a phase-locked loop (PLL).

The properties of the selected sensorless method must be taken into account during system design. Since the injection-based methods are expected to be applied at low angular speed region, basically two main challenges must be solved. One of them is the initial angle estimation, which is necessary if the encoder, on which the vector control depends at higher angular speed regions, is not capable of providing absolute angle information. This can be achieved without rotating the motor [9], [10] which usually requires the motor parameters, or during rotation, with a vibration method [11] - [13]. The other challenge is the transition between the sensorless and sensored vector control.

Based on the authors previous works the multiphysical approach provides optimal design of the drive system [14], [15]. The integration of the FEM analysis results in the drive control algorithm development provides more precise machine parameters, which can be taken into account in the form of look-up tables depending on the actual current, temperature or frequency. On the other hand, these results allow seeking the limitation and boundaries of stability of the applied control method.

The authors investigate the high-frequency, synchronous voltage injection method applied on PMSMs. The research of the method requires a machine model, which was obtained as a combination of the FEM analyses results and the machine's space vector-based differential equations. The authors motivation with this modeling approach was to obtain a fast running, and yet precise enough modeling of the custom designed PMSM. The machine modeling and its steps are presented in Section 2.

This is followed by the detailed description of the high-frequency synchronous voltage injection method in Section 3. The investigated estimator structure is based on a Phase-Locked Loop (PLL). During the modeling and also the literature overview the authors realized that no proper description of the PLL's PI controller's tuning was published or detailed. In this paper, the authors present a new dynamic model making possible the tuning of the PLL-based estimator structure. Since the machine's FEM analysis was carried out in the previous section, the authors used its results and combined it with this new, proposed dynamic model. With the combination of these two, the authors were able to investigate deeper proposed method's limitations including stability analysis for the estimator structure's controller.

Section 4 presents the simulation and experimental measurement results. The sensorless control method, along with the machine model was validated with the experimental drive setup, developed by the authors. The whole control software investigation was carried out using the model-based development methodology, where the same model was used for the simulations and also for the embedded software development.

2 FEM Analysis and Modeling of PMSM

The target of the analysis was to obtain the machine parameters in the form of look-up tables. These results were used to create a machine model, which involves saturating effects. Such machine model offers significantly faster simulation speed compared to coupled simulations with enough accuracy and precision for the drive control algorithm development. The obtained FEM results were also used to investigate the applied algorithms limitations and stability, which are presented in Section 3.

2.1 Finite Method Analysis

The performed rotating machine analysis was the combination of measurement data evaluation and finite element method (FEM) analysis, so standard no-load and nominal load and short-circuit measurements were performed on the custom designed PMSM. Table 1 summarizes the motor parameters and their source.

Table 1
Permanent Magnet Synchronous Machine Design Parameters

Parameter	Value	Source
P_n	$2kW$	Design parameter
U_n	$330V$	Design parameter
I_n	$3.5A_{RMS}$	Nominal load measurement
n_n	$3000RPM$	Design parameter
R	2.71 Ω	RLC measurement
Ψ_p	$0.335\ Vs$	No-load measurement
p	2	Design parameter
J	$0.0036\ kgm^2$	Design parameter
F	$0.0011\ Nms$	Design parameter

The inputs of the FEM analysis were the known motor topology including the applied materials and winding scheme. In the first step the $\boldsymbol{d-q}$ axes fluxes were calculated, which are the functions of direct-axis $\boldsymbol{i_d}$ and quadrature-axis $\boldsymbol{i_q}$ currents. During the analysis, and later in the space vector-based machine model, the $\boldsymbol{d}$ axis was bound to the rotor's circumferential flux density distribution's positive peak.

In the flux calculation's first setup, the rotor was set into $\alpha_{elec} = 0deg_e$ position, as shown in Fig. 1(a), to calculate the d axis flux $\Psi_d(i_d, i_q)$. In the second setup the rotor was positioned in $\alpha_{elec} = 90deg_e$ direction, as shown in Fig. 1(b), in order to calculate progression of q axis flux $\Psi_q(i_d, i_q)$. For both cases all the possible $\bar{\imath} = i_d + ji_q$ combinations were examined on the $[-2\hat{I}_n \ \ 2\hat{I}_n]$ current interval with $\Delta i = 0.4A$ resolution, and the result are shown in Fig. 3(a) and (b) for the selected machine.

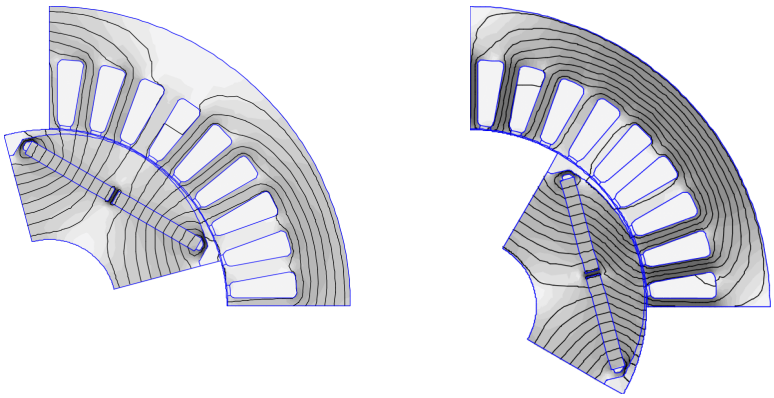

(a) (b)

Figure 2
Flux and inductance calculation in (a) $\alpha_{elec} = 0deg_e$ direction alignment, (b) $\alpha_{elec} = 90deg_e$ direction alignment

With the known progression of $\Psi_d(i_d, i_q)$ and $\Psi_q(i_d, i_q)$ fluxes the self- and cross-coupling inductances could be calculated [16], [17]. Since the fluxes are calculated discrete points, the partial derivative's approximation was used in the post process calculations, so

$$L_d(i_d, i_q) = \frac{\partial \Psi_d(i_d,i_q)}{\partial i_d} \approx \frac{\Delta \Psi_d(i_d,i_q)}{\Delta i_d}\Big|_{i_q = \text{ const.}}, \quad (1)$$

$$L_{dq}(i_d, i_q) = \frac{\partial \Psi_d(i_d,i_q)}{\partial i_q} \approx \frac{\Delta \Psi_d(i_d,i_q)}{\Delta i_q}\Big|_{i_d = \text{ const.}}, \quad (2)$$

$$L_q(i_d, i_q) = \frac{\partial \Psi_q(i_d,i_q)}{\partial i_q} \approx \frac{\Delta \Psi_q(i_d,i_q)}{\Delta i_q}\Big|_{i_d = \text{ const.}}, \quad (3)$$

$$L_{qd}(i_d, i_q) = \frac{\partial \Psi_q(i_d,i_q)}{\partial i_d} \approx \frac{\Delta \Psi_q(i_d,i_q)}{\Delta i_d}\Big|_{i_q = \text{ const.}}. \quad (4)$$

where L_d is the direct axis self-inductance, L_{dq} is the quadrature-to-direct axis cross-coupling inductance, L_q is the quadrature axis self-inductance and L_{qd} is the direct-to-quadrature axis cross-coupling inductance. Based on these calculations the nominal values of L_d and L_q are $15.06\ mH$ and $36.23\ mH$ respectively.

The machine's torque profile was calculated over two pole pitches on the $[0\ 2\hat{I}_n]$ interval with $\Delta i = 1A$ and $\Delta\alpha_{elec} = 1deg_e$ resolutions and its results are shown in Fig. 3(g).

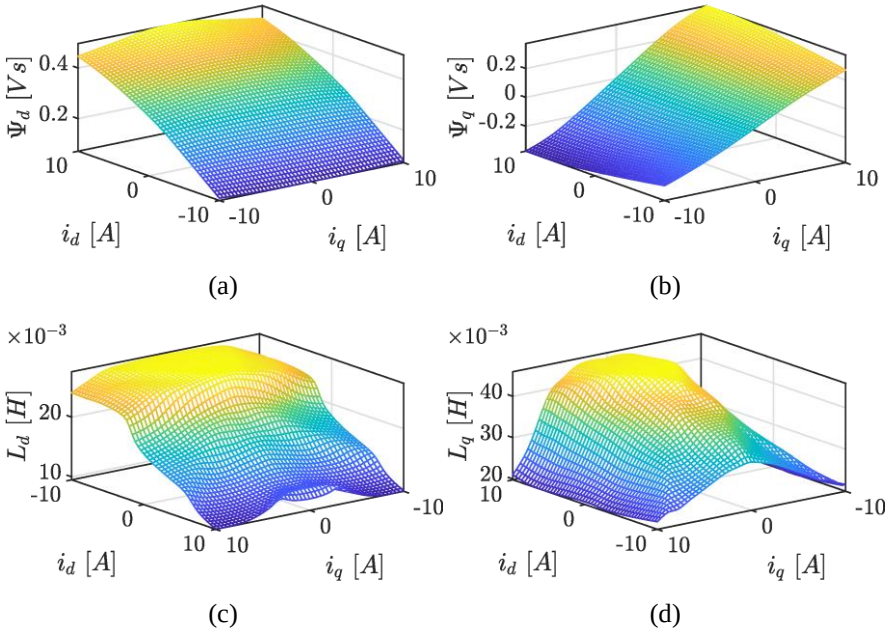

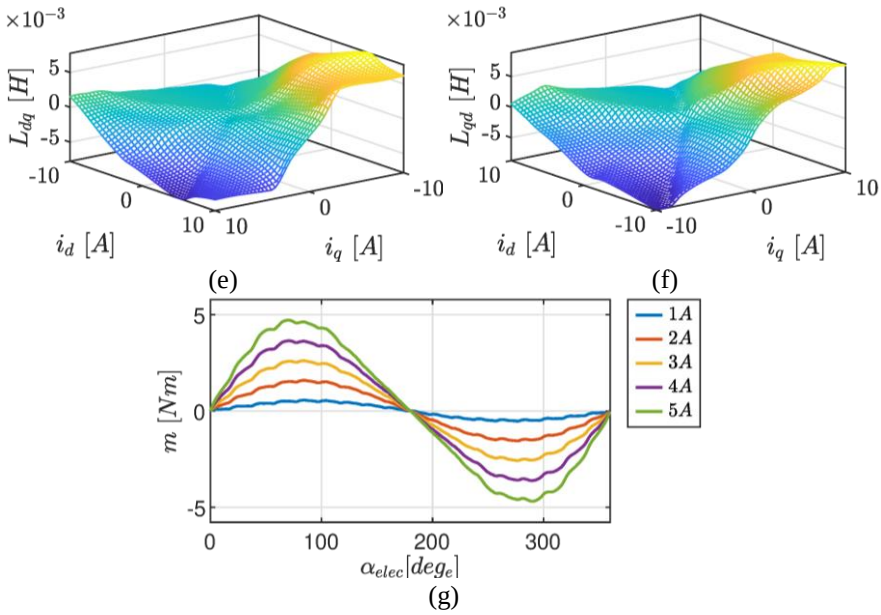

Figure 3

FEM analysis results (a-b) progression of fluxes (c-f) progression of fluxes inductances (g) torque profile

The cogging torque of the motor was modelled as the difference of the FEM calculated torque and the saturating lumped-element model's torque. In the machine model it was taken into account using a look-up table, which is the function of current amplitude and actual electric rotor position, as shown in Fig. 4. The intermediate points were calculated with interpolation. The peaks in the modelled cogging torque can be observed around the reluctance torque's peak and also in highly saturated cases. These deviations come from the inaccuracy of the FEM software's calculation since the motor parameters were derived from its results.

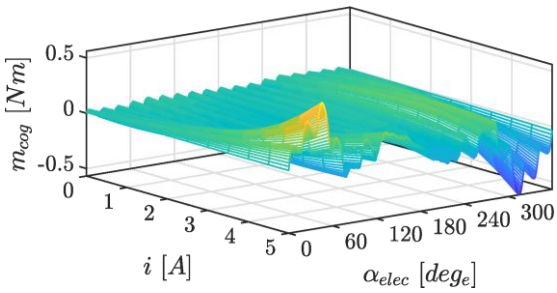

Figure 4

Cogging toque lool-up table in a function of current amplitude and electric angle

2.2 Mathematical Model of Permanent Magnet Synchronous Machine

Equations (5)-(8) show the system of equations, which models the machine in the $d-q$ frame, whilst Fig. 5 shows the space vector-based equivalent circuit of the machine. In this figure $\bar{\bar{L}}$ denotes the 2×2 diagonal stator inductance matrix, which contains the d- and q-direction inductances and cross-coupling inductances that were obtained using FEM analysis and which are shown in Fig. 3(c-f).

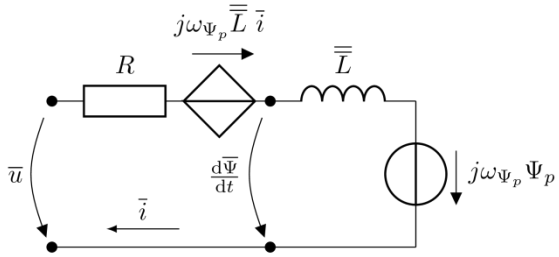

Figure 5
Equivalent circuit of permanent magnet synchronous machine

$$u_d = Ri_d + L_d \frac{di_d}{dt} + L_{dq} \frac{di_q}{dt} - \omega_{\Psi_p}(L_{qd} i_d + L_q i_q)\,, \tag{5}$$

$$u_q = Ri_q + L_q \frac{di_q}{dt} + L_{qd} \frac{di_d}{dt} + \omega_{\Psi_p}(L_d i_d + L_{dq} i_q + \Psi_p)\,, \tag{6}$$

$$m = \frac{3}{2} p \left(\left(L_d - L_q\right) i_d i_q + L_{dq} {i_q}^2 - L_{qd} {i_d}^2 + \Psi_p i_q \right) + m_{cog}\,, \tag{7}$$

$$\Theta \frac{d\omega}{dt} = m - m_l - F\omega\,, \tag{8}$$

where u_d and u_q are the real and imaginary parts of the corresponding voltage space vector, R is the stator resistance, i_d is i_q are the real and imaginary parts of the corresponding current space vector, m_{cog} is the cogging torque, m is the machine's electromagnetic torque, m_l is the load torque on the shaft, Θ is the rotor's moment of inertia, F is the friction loss factor, p is the number of pole pairs, ω is the shaft angular speed and ω_{Ψ_p} is the electric angular speed where $\omega_{\Psi_p} = p\omega$.

3 High-Frequeny Injection Methods on PMSMs

3.1 High Frequency Synchronous Injection

In case of high frequency synchronous injection, the test vectors are injected in the estimated $\hat{d} - \hat{q}$ frame shown in Fig. 6. This figure also explains the angle relations, which are used during the modeling process; based on Eq. (9), the angle

displacement between the real and estimated coordinate systems is considered positive, if the estimated angle lags behind the real one, so

$$\alpha_{err} = \alpha_{\Psi_p} - \hat{\alpha}_{\Psi_p} , \tag{9}$$

where α_{Ψ_p} is pole flux vector's angle, $\hat{\alpha}_{\Psi_p}$ is its estimated value. In the following, the hat symbol (ˆ) will denote the estimated values, h subscripts will refer to high frequency components.

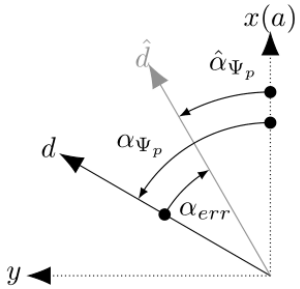

Figure 6
Angle relations between the real and estimated coordinate systems

The injected voltages are expected to positive sequence set of harmonic signals, so Eq. (10) shows both time and complex frequency domain components, where the complex rotating vector was bound to the sine wave.

$$\begin{bmatrix}\hat{u}_{dh}\\ \hat{u}_{qh}\end{bmatrix} = \begin{bmatrix}u_h \sin(\omega_h t)\\ -u_h \cos(\omega_h t)\end{bmatrix} = \begin{bmatrix}u_h\\ -ju_h\end{bmatrix} , \tag{10}$$

where $\hat{u}_{dh}$ and $\hat{u}_{qh}$ are the injected voltages in the estimated $\hat{d}$- and $\hat{q}$-directions, u_h is the amplitude of the injected voltages, $\omega_h = 2\pi f_h$, where f_h is the injection frequency, j is the imaginary unit.

In a real drive system, the measurements can only be performed in the stationary reference frame. Accordingly, the high-frequency stationary current vector components can be expressed as follows,

$$\begin{bmatrix}i_{xh}\\ i_{yh}\end{bmatrix} = \bar{\bar{R}}^{-1}\left(\alpha_{\Psi_p}\right) \bar{\bar{Z}}^{-1}{}_h \bar{\bar{R}}(\alpha_{err}) \begin{bmatrix}\hat{u}_{dh}\\ \hat{u}_{qh}\end{bmatrix}, \tag{11}$$

where i_{xh} and i_{yh} are the real and imaginary parts of the corresponding high-frequency stationary current space vector, $\bar{\bar{R}}(\alpha)$ is the rotational operator for any given angle, $\bar{\bar{Z}}_h$ is the high frequency impedance matrix of the machine. This impedance matrix can be derived from the machine equations Eqs. (5)-(8) and should be written in the following form,

$$\bar{\bar{Z}}_h = \begin{bmatrix} R + j\omega_h L_d - \omega_{\Psi_p} L_{qd} & j\omega_h L_{dq} - \omega_{\Psi_p} L_q \\ j\omega_h L_{qd} + \omega_{\Psi_p} \left(L_d + \frac{\Psi_p}{i_d}\right) & R + j\omega_h L_q + \omega_{\Psi_p} L_{dq} \end{bmatrix} \approx$$
$$\begin{bmatrix} R + j\omega_h L_d & 0 \\ 0 & R + j\omega_h L_q \end{bmatrix} = \begin{bmatrix} \bar{Z}_{h11} & 0 \\ 0 & \bar{Z}_{h22} \end{bmatrix}. \quad (12)$$

Equation (12) shows that during the modeling some simplifications can be performed. The $\omega_{\Psi_p} L_{qd}$ and $\omega_{\Psi_p} L_{dq}$ terms in the main diagonal and also the anti-diagonal elements can be neglected since their contribution to the current response is much smaller than the others'.

3.2 Signal Processing

In most cases a Phase-Locked-Loop (PLL) structure is used, which block diagram is illustrated in Fig. 7.

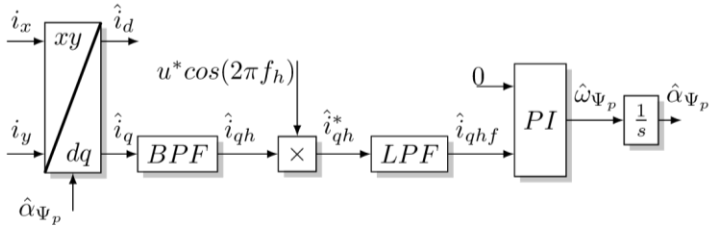

Figure 7
PLL structure used for angle estimation

In the first step of the estimation, the measurable stationary coordinate system currents are transformed into the estimated reference frame. Thereafter, they are filtered off using a BPF where BPF is the abbreviation for band-pass-filter, which lets through the current components around the injection frequency region. These operations in Eq. (13), which shows the high-frequency components.

$$\begin{bmatrix} \hat{i}_{dh} \\ \hat{i}_{qh} \end{bmatrix} = \bar{\bar{R}}\left(\hat{\alpha}_{\Psi_p}\right) \begin{bmatrix} i_{xh} \\ i_{yh} \end{bmatrix}, \quad (13)$$

where

$$\hat{i}_{dh} = (cos^2(\alpha_{err})\bar{Y}_{11} + sin^2(\alpha_{err})\bar{Y}_{22})\hat{u}_{dh}$$
$$+ \sin(\alpha_{err}) \cos(\alpha_{err}) (\bar{Y}_{11} - \bar{Y}_{22}) \hat{u}_{qh}\,, \quad (14)$$
$$\hat{i}_{qh} = \sin(\alpha_{err}) \cos(\alpha_{err}) (\bar{Y}_{11} - \bar{Y}_{22}) \hat{u}_{dh}$$
$$+ (sin^2(\alpha_{err})\bar{Y}_{11} + cos^2(\alpha_{err})\bar{Y}_{22})\hat{u}_{qh}\,, \quad (15)$$

where $\bar{Y}_{11} = \frac{1}{\bar{Z}_{h11}}$, $\bar{Y}_{22} = \frac{1}{\bar{Z}_{h22}}$ and for latter expressions $\varphi_{11} = arc(\bar{Y}_{11})$, $\varphi_{22} = arc(\bar{Y}_{11})$.

In most of the cases only $\hat{u}_{dh}$ is injected, therefore, only the tracking of $\hat{\imath}_{qh}$ would be enough, and it can be reduced to,

$$\hat{\imath}_{qh} = \sin(\alpha_{err})\cos(\alpha_{err})\,(\bar{Y}_{11} - \bar{Y}_{22})\,\hat{u}_{dh}\ , \tag{17}$$

which is a complex phasor and its equivalent time signal is shown in Eq. (18).

$$\hat{\imath}_{qh}(t) = u_h \sin(\alpha_{err})\cos(\alpha_{err})\,|\bar{Y}_{11} - \bar{Y}_{22}|sin\big(\omega_h t + arc(\bar{Y}_{11} - \bar{Y}_{22})\big) \tag{18}$$

This signal is fed into the phase detector, where it is multiplied with a cosine function having the same frequency as the injected voltage and amplitude u^*. The phase detector's output can be split into two components. One of these components is a DC-like quantity, whilst the other has twice frequency as the injection one. The latter can be filtered off using a Low-Pass-Filter, referred as *LPF* in Fig. 7, resulting $\hat{\imath}_{qhf}(t)$, as shown in Eq. (19).

$$\hat{\imath}_{qhf}(t) \approx \tfrac{1}{2} u_h u^* \sin(\alpha_{err})\cos(\alpha_{err})\,|\bar{Y}_{11} - \bar{Y}_{22}|sin\big(arc(\bar{Y}_{11} - \bar{Y}_{22})\big)\,. \tag{19}$$

$\hat{\imath}_{qhf}(t)$ is fed into the PLL's PI controller as a feedback signal, and the controller's reference is set to zero. Observing Eq. (19) the feedback signal can be zero in four possible ways:

1) u_h or u^* equals zero,
2) $|\bar{Y}_{11} - \bar{Y}_{22}|$ becomes zero. In this case, the machine is fully symmetrical in magnetic point of view, so no high frequency signal injection methods can be applied,
3) $arc(\bar{Y}_{11} - \bar{Y}_{22})$ becomes zero, which also means that the high frequency impedances are equal,
4) $\sin(\alpha_e)\cos(\alpha_e)$ becomes zero. This can be observed, when α_{err} equals zero, which represents full alignment with the d axis, or when α_{err} equals $\pm\pi$, in which case the estimator finds the -d axis. Furthermore, two more solutions come form the $\alpha_e = \pm\frac{\pi}{2}$ cases , representing full alignment with $\pm q$ axes. In case of synchronous injection, the initial angle error should be within $\left]-\frac{\pi}{2}\ \frac{\pi}{2}\right[\ rad_e$ interval.

3.2 Dynamic Model for the PLL Structure

The tuning of PLL's controller requires a dynamic model, which can be created with the respect of the estimator structure. Equations (13)-(19) are valid in steady state since phasors were involved in the calculations, but these results can be used to obtain the dynamic model. The proposed closed loop structure is illustrated in Fig. 8.

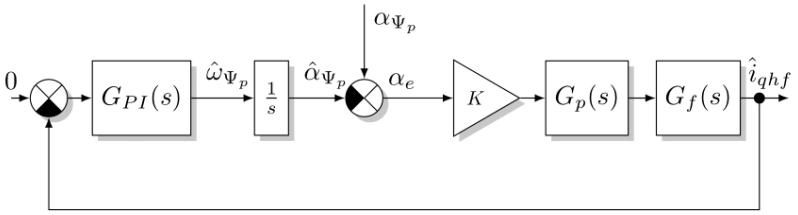

Figure 8
Proposed dynamic model for the PLL-based estimator

$G_{PI}(s)$ denotes a PI type controller, which was taken into account with the ideal form, so

$$G_{PI}(s) = A_p\left(1+\frac{1}{sT_i}\right), \tag{20}$$

where A_p is the proportional gain, T_i is the integral time.

$G_p(s)$ denotes the plant's transfer function, which is created using both d- and q-direction R-L circuits and it can be expressed as

$$G_p(s) = \frac{p_1 s^2+p_2 s+p_3}{(s-\lambda_d)(s-\lambda_q)}, \tag{21}$$

where

$$p_1 = -\frac{|\bar{Y}_{11}|\sin(\varphi_{11})}{\sin(\varphi_{11}+\varphi^*)}+\frac{|\bar{Y}_{22}|\sin(\varphi_{22})}{\sin(\varphi_{11}+\varphi^*)}+c=0, \tag{22}$$

$$p_2 = -\frac{|\bar{Y}_{11}|\sin(\varphi_{11})}{\sin(\varphi_{11}+\varphi^*)}\frac{R}{L_q}+\frac{|\bar{Y}_{22}|\sin(\varphi_{22})}{\sin(\varphi_{11}+\varphi^*)}\frac{R}{L_d}+c\frac{R}{L_d}+c\frac{R}{L_q}, \tag{23}$$

$$p_3 = c\frac{R^2}{L_d L_q}, \tag{24}$$

and the auxiliary variables are

$$c = \sqrt{|\bar{Y}_{11}|^2+|\bar{Y}_{22}|^2-2|\bar{Y}_{11}||\bar{Y}_{22}|\cos(\varphi_{22}-\varphi_{11})}, \tag{25}$$

$$\varphi^* = \tan^{-1}\left(\frac{-|\bar{Y}_{22}|\sin(\varphi_{22}-\varphi_{11})}{|\bar{Y}_{11}|+|\bar{Y}_{22}|\cos(\varphi_{22}-\varphi_{11})}\right). \tag{26}$$

In the last step K gain can be defined based on the PLL's phase detector part and Eq. (19), so

$$K = \frac{1}{2}u_h\, u^* sin\left(arc(\bar{Y}_{11}-\bar{Y}_{22})\right) = \frac{1}{2}u_h\, u^* sin(\varphi_{11}+\varphi^*). \tag{27}$$

$G_f(s)$ denotes the loop filter of the PLL, which is used to a be a simple low pass filter with the following form

$$G_f(s) = \frac{\omega_{c,LPF}}{s+\omega_{c,LPF}}, \tag{28}$$

where $\omega_{c,LPF}$ is the low-pass filter's cut off frequency. Thereafter, the $G_o(s)$ open loop transfer function of the dynamic model can be modeled as shown in Eq. (29).

$$G_o(s) = -KA_p\left(1+\frac{1}{sT_i}\right)\frac{1}{s}\frac{p_1s^2+p_2s+p_3}{(s-\lambda_d)(s-\lambda_q)}\frac{\omega_{c,LPF}}{s+\omega_{c,LPF}} \ . \tag{29}$$

3.3 Parameter Sensitivity and Stability Analysis

The proposed new dynamic model of the system depends on the machine parameters that can change during operation, therefore, their effect on the system stability must be investigated. The investigation was carried out assuming the following conditions:

- industrial grade temperature range, staring from $-40\ C^{\circ}$representing the worst-case cold start, till $155\ C^{\circ}$ which is the maximum allowed hot-spot temperature in case of the widely used F insulation class. The range of inspection is [2.0331 Ω ÷ 4.1258 Ω] and it was used to model the stator resistance change and its effect on the system,
- the saturation of L_d, L_q inductances, which are the functions of the $d-q$ axes currents.

The stability analysis focused on the estimator structure's performance deviation due to the machine parameters changes.

Table 2
Injection, filter and controller parameters for high-frequency synchronous injection on PMSM

Parameter	Value
u_h	$10V$
f_h	$500Hz$
$\omega_{c,LPF}$	$2\pi 50 rad/s$
A_p	2350
T_i	$23{,}5s$

Table 2 summarizes the injection parameters and also the PI controller's ones which were used in the synchronous injection method. With the help of the proposed dynamic model, the tuning of the PLL's PI controller can be performed. The tuning was based on the nominal values of the motor parameters, and the PI controller's parameters are chosen to achieve $\varphi_m = 45\ deg_e$ phase margin in the open loop Bode diagram shown in Eq. (29), and its results are shown in Fig. 9. This setup gives balance between the stability and the step response's overshoot and time constant. The estimator's PI controller's objective is to force down $\hat{\imath}_{qhf}(t)$ to zero since in that case full alignment with the real and estimated coordinate system's angle can be achieved. In the next step the possible limits of the injection method and drive system were defined, which were the following:

- L_q/L_d ratio must be above 1.2 . It is required since the method is based on the impedance difference between the $d-q$ axes impedances,
- the stator current must be kept below its allowed maximum. During the investigation $\sqrt{i_d^2+i_q^2} < 1.5\sqrt{2}I_n$ limit was defined.

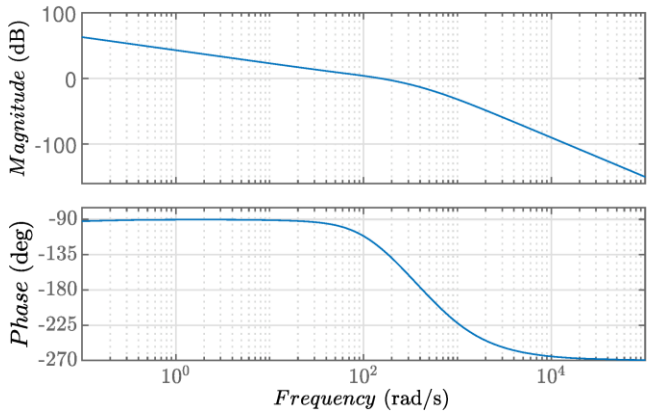

Figure 9

Open loop Bode diagram of the proposed estimator assuming nominal motor parameters

With the respect of these limits, the prohibited L_d, L_q inductance combinations are presented in Fig. 10.

The inspection of Fig. 11 shows the possible current combinations allowed for controlled electric drive, using the high-frequency synchronous injection. Beside the classic current limit, referred as *Motor Current limit* which is meant to protect the machine from sever overload conditions, the predefined minimum allowed ratio of the inductances decreases further the allowed current vector combinations.

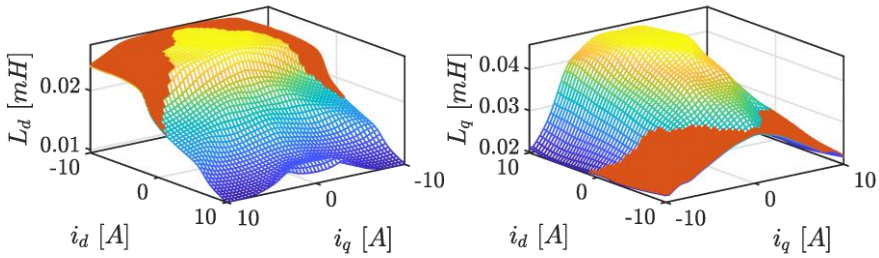

(a) (b)

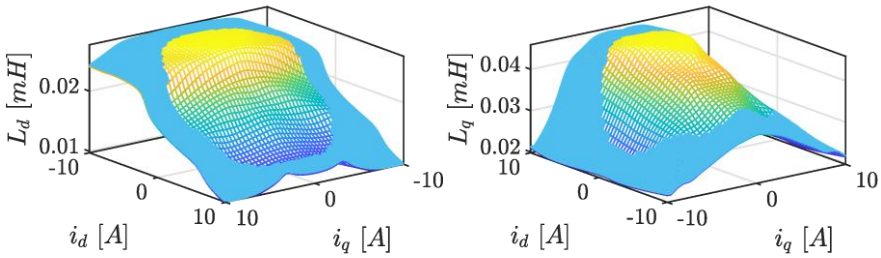

(c) (d)

Figure 10

Prohibited current regions (a)(b) L_d, L_q inductances considering L_q/L_d > 1.2 ratio (in (b) i_d axis is mirrored), (c)(d) L_d, L_q inductances considering $\sqrt{i_d^2 + i_q^2} < 1.5\sqrt{2}I_n$ limit (in (d) i_d axis is mirrored)

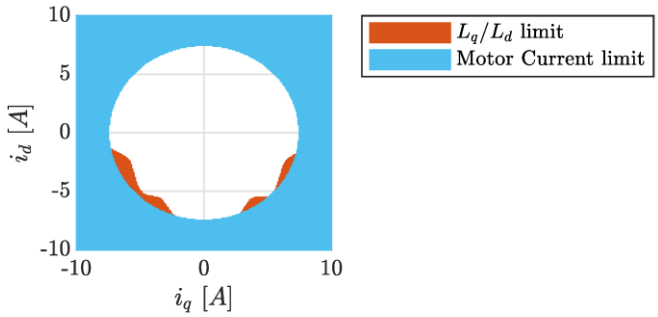

Figure 11

Current limits

The additional limitation occurs mostly at negative d-axis current basically affects two commonly used algorithms. The first one is the *Maximum-Torque-Per-Ampere* (MTPA) [18] which tries to utilize the machine torque more efficient way by involving the reluctance torque too. In case of the machine under test the MTPA algorithm could use these negative d-axis currents in positive motoring directions since the $L_q > L_d$. The second affected algorithm is the field weakening logic [19], which also requests negative d-axis current reference if the rotor speed demand is above nominal. In most of the cases the high frequency injection methods are applied in low- speed region, therefore, these limitations will not be a problem.

With the defined current limits, the stability analysis of the proposed method could be performed. This analysis included all the possible combinations of the stator resistance and $i_d > i_q$ currents, thus L_d, L_qvalues. For each combination φ_m phase margin of the system was calculated and its progression for two stator resistance values are summarized in Fig. 12.

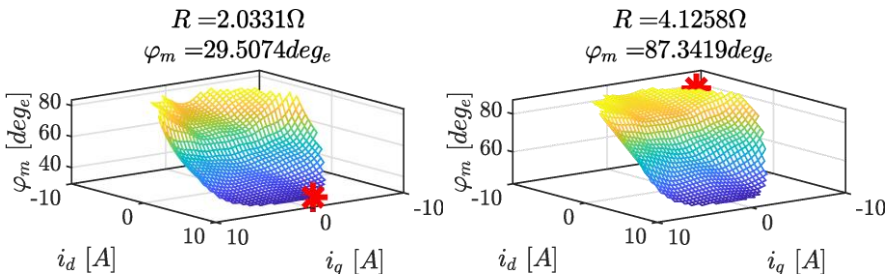

(a) (b)

Figure 12

Progression of the phase margin (a) with the lowest stator resistance resulting the minimum phase margin, (b) with the highest stator resistance resulting the maximum phase margin

Figure 12 clearly shows that within the allowed current limits the system is stable. The phase margin has its absolute minimum value, $\varphi_m = 29.5074\ deg_e$ on the range of inspection when the stator resistance had its minimal value, $R = 2.0331\ \Omega$. This could be observed at cold start, when the machine is cooled down to $-40\ C^\circ$. Thereafter, if the machine heats up, making the stator resistance to increase, the control system becomes more stable. This makes the system to have its maximal phase margin of $\varphi_m = 87.3419\ deg_e$ at the highest allowed temperature with stator resistance of $R = 4.1258\ \Omega$. The phase margin's maximum and minimum can be observed at highly saturated cases, furthermore its minimum occurs when d-axis current is positive and high. These current combinations could happen during high dynamic loaded conditions with applied MTPA algorithm. In parameter point of view, the inductances could be considered sensitive parameters since in both 12(a)(b) the phase margin changes the most due their saturations. The proposed dynamic system's stability can be maintained with simple current limitations, which highly simplifies the implementation of a vector-controlled system with high frequency synchronous injection. The possible affected additional algorithms, such as MTPA or field-weakening, just need to be expanded with current limit look-up table, as shown in Fig. 11, and it can be calculated based on the post-process of the FEM results.

4 Simulation Results and Experimental Results

The simulations were run in MATLAB Simulink, and the measurements were performed on a 2 kW ST STGIPS20C60 IGBT-based single phase input inverter, which was controlled with an isolated TMS320F28397D-based control module as shown in Fig. 13.

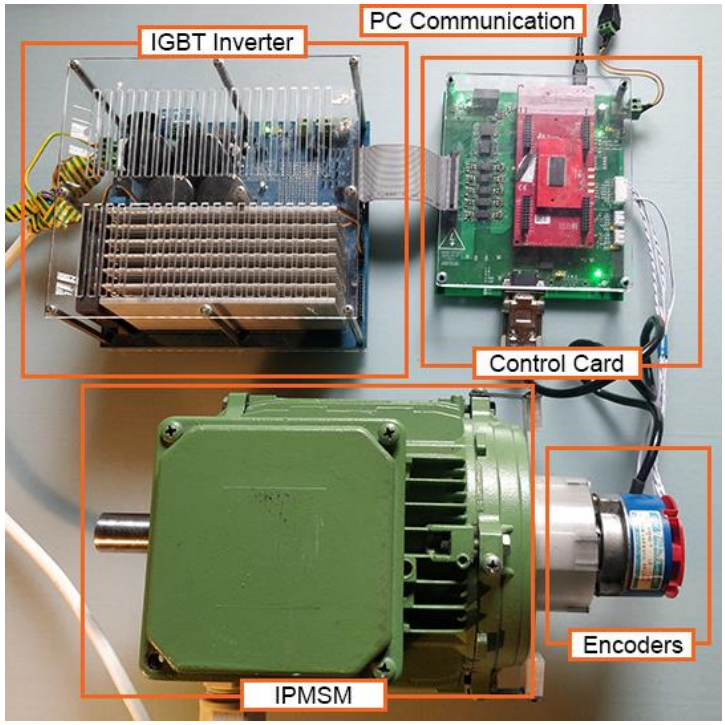

Figure 13
Experimental inverter setup

The PMSM under test was equipped with two encoders as shown in Fig. 14. The first one was a TLE5009 contactless SINCOS encoder which was used for validation of the calculated common coordinate system's angle. The other one, used for the vector control, was a Tamagawa Seiki TS5208N458 shaft mounted incremental encoder

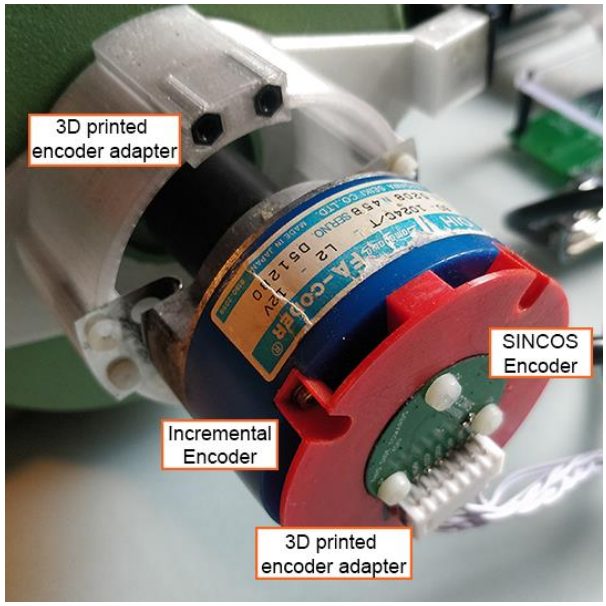

Figure 14
Dual encoder configuration

The drive control's objective was to achieve the user's speed request by governing the appropriate currents for that. There are many successfully applied approaches in the literature, such as Model Predictive Control (MPC) [20]-[21], or Reinforcement-Based Learning controls [22], but not least the widely used PI cascade structure. The authors selected the latter one because of its ease of implementation. The control structure used in the simulations and the experimental measurements is illustrated in Fig. 15.

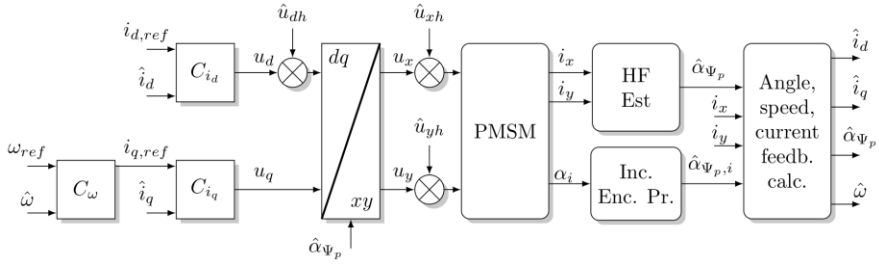

Figure 15
Cascade control loop

All of the controllers, C_{i_d}, C_{i_q} and C_ω are PI type controllers, and they were modeled as PD Integral PI controllers to handle the controller saturation and anti-windup requirements in the discrete time drive software [23]–[25]. Table 3 summarizes the

controller parameters, which were obtained using the predefined cut-off frequencies and damping factors method with the respect of the estimator's cut-off frequency.

Table 3
Controller parameters and filter time constants

Parameter	Value	Description
$A_{p,d}$	0.1	d-direction current controller proportional gain
$T_{i,d}$	0.5	d-direction current controller integral time
$A_{p,q}$	2	q-direction current controller proportional gain
$T_{i,q}$	5	q-direction current controller integral time
$A_{p,\omega}$	0.2	angular speed controller proportional gain
$T_{i,\omega}$	200	angular speed controller integral time

The *PMSM* block represents the saturating, lumped-parameter permanent magnet synchronous machine model, and its parameters were obtained by the calculation presented in Section 2. The *Inc. Enc. Proc.* block handles the incremental encoder by the microcontroller's enhanced *Quadrature Encoder Pulse* (eQEP) module, and it also handles the SINCOS encoder, which outputs were routed into the microcontroller's AD module. The PWM switching and also the control algorithm's sampling frequencies were set to $10\ kHz$. The measurement results were recorded by the control card in SDRAM using *External Memory Interface* (EMIF).

The *HF Estimators* block includes the two sensorless methods, where the stationary injection method was used for the initial angle estimation, whilst the synchronous injection method was used to estimate the common coordinate system's angle below $20\ Hz$ electric frequency.

The *Angle, speed, current feedback calc*. block calculates the feedback signals and also handles the transition between the sensorless method's estimated angle and the incremental encoder's angle.

During the test cycle no-load condition was examined, where the cogging torque effects expected to be the highest comparing to the dynamic torque. The authors wanted to demonstrate that the sensorless method is capable of providing good estimation, even though the relatively high current and torque ripples.

Figures 15 and 16 summarize the simulation results and also the experimental test results. The same scenario was programmed in the simulation and into the inverter to obtain comparable results. Figures 15(a) and 16(a) show the actual state of the angle estimation, through $AngleSource$. During its $Stat$ value the angle estimation was performed by the stationary injection, which was used in the initial state of the motor control algorithm [26]. The stationary injection lasted $200\ ms$, which was

followed by a $200\,ms$ long wait state. Thereafter, in $Synch$ state angle was estimated with the synchronous injection method, until the frequency remained below $20\,Hz$ electric. This was followed by a $Tr1$ transition state, when the motor control became sensored, and the high-frequency signal injection ended. The Enc state represents the sensored vector control region, when the position of the common coordinate systems was fully calculated by using the incremental encoder. The $Tr2$ state represents and other transitioning state, between the sensored and sensorless method.

Figures 15(b-c) and 16(b-c) show the simulated and measured $d-q$ currents and their references. The progression of the currents is similar, but the measurements showed slightly higher ripples. Beside the higher ripples in the measured q-direction current, its progression in the generator region also slightly differs. This deviation comes from mechanical model's inaccuracy. This can be improved by involving a more precise velocity-based friction torque model, which is used to be the sum of the Stribeck, Coulomb, and viscous torque components. Together with Figs. 15(d) and 16(d) the frequency regions can be seen where the injection methods were active. These figures also show the speed control performance of the cascade loop. The controller was able to follow the reference in both clockwise and counter clockwise directions, even in low-speed region, where the angle and also the speed calculation was performed with the sensorless method. The transition states were also successful in both sensorless to sensored and the opposite case too.

Figures 15(e) and 16(e) show the high frequency $d-q$ current components, which were obtained using a BPF. They clearly show when the sensorless methods were active.

Figures 15(f) and 16(f) show the angle estimation errors. These results were obtained using the additional SINCOS encoder as a calibrated reference angle source. In the simulations the stationary injection was able to find the real d axis with $0.0659\,rad_e = 3.7758\,deg_e$ precision. Based on Eq. (19) this precision is fair enough, since the initial angle error is required to be within the $\left]-\frac{\pi}{2}\ \frac{\pi}{2}\right[\,rad_e$ interval. Thereafter, when the synchronous injection became active and the motor was in still state, it fell to $0.0027\,rad_e = 0.1547\,deg_e$. During movement the maximum estimation error was $0.08209\,rad_e = 4.703\,deg_e$. During the sensored vector control, which is called Enc state in Fig. 15(a), the angle error remained the last error value at the end of the transition state. The same progression can be observed in the measurements, but with slightly higher noise. The initial angle estimation's precision was $0.1323\,rad_e = 7.5802\,deg_e$. Thereafter the synchronous injection's PLL was able to estimate the angle around zero average value. During movement, when the rotation started the error jumped up to $0.1348\,rad_e = 7.7234\,deg_e$ but thereafter it was around $0.05416\,rad_e = 3.103\,deg_e$, with $\pm\,0.02\,rad_e = 1.1459\,deg_e$ estimation noise.

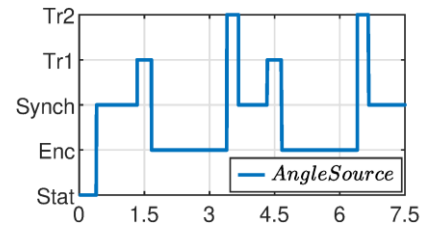
Tr2
Tr1
Synch
Enc
Stat
AngleSource
0
1.5
3
4.5
6
7.5

(a)

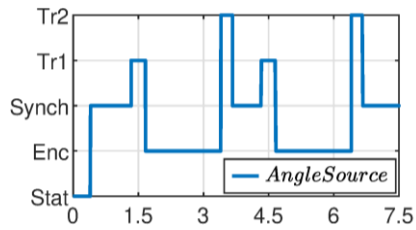
Tr2
Tr1
Synch
Enc
Stat
AngleSource
0
1.5
3
4.5
6
7.5

(a)

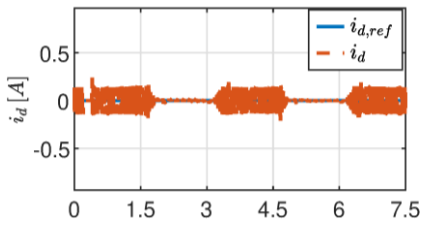
$i_{d,ref}$
i_d
$i_d\,[A]$
0.5
0
-0.5
0
1.5
3
4.5
6
7.5

(b)

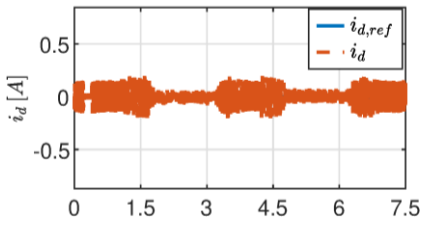
$i_{d,ref}$
i_d
$i_d\,[A]$
0.5
0
-0.5
0
1.5
3
4.5
6
7.5

(b)

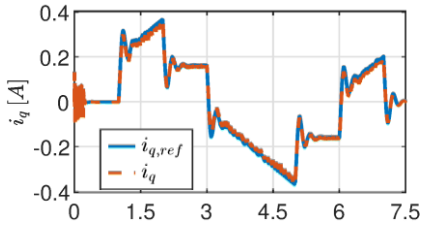
$i_{q,ref}$
i_q
$i_q\,[A]$
0.4
0.2
0
-0.2
-0.4
0
1.5
3
4.5
6
7.5

(c)

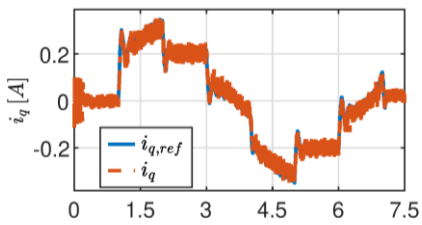
$i_{q,ref}$
i_q
$i_q\,[A]$
0.2
0
-0.2
0
1.5
3
4.5
6
7.5

(c)

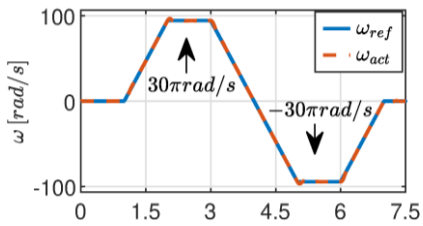
ω_{ref}
ω_{act}
$30\pi rad/s$
$-30\pi rad/s$
$\omega\,[rad/s]$
100
0
-100
0
1.5
3
4.5
6
7.5

(d)

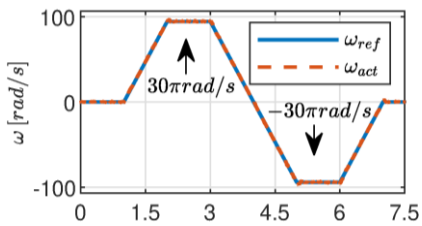
ω_{ref}
ω_{act}
$30\pi rad/s$
$-30\pi rad/s$
$\omega\,[rad/s]$
100
0
-100
0
1.5
3
4.5
6
7.5

(d)

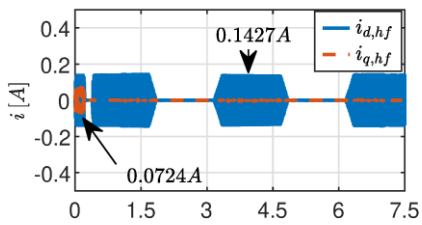
$i_{d,hf}$
$i_{q,hf}$
$0.1427A$
$0.0724A$
$i\,[A]$
0.4
0.2
0
-0.2
-0.4
0
1.5
3
4.5
6
7.5

(e)

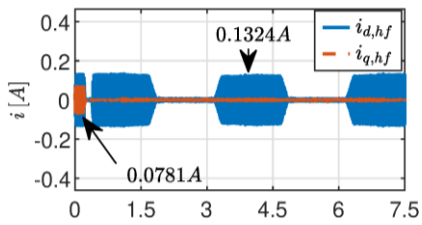
$i_{d,hf}$
$i_{q,hf}$
$0.1324A$
$0.0781A$
$i\,[A]$
0.4
0.2
0
-0.2
-0.4
0
1.5
3
4.5
6
7.5

(e)

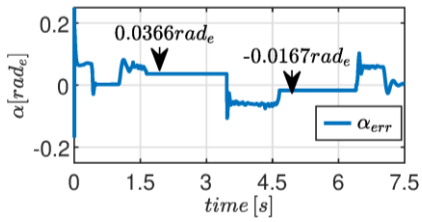

(f)

Figure 15
Simulation results

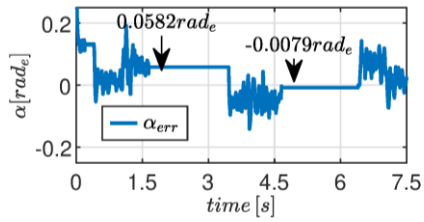

(f)

Figure 16
Experimental measurement results

Conclusions

This paper presented the sensorless vector control of a custom made PMSM using high-frequency synchronous injection. In the first step of the investigation the FEM analysis of the machine was performed, and its output was later used in the creation of the machine model and also during the stability analysis. The presented machine model gave precise and fast results confirmed by the experimental measurement results. An improvement of the model can be a better mechanical model, which models better the velocity-based friction torques.

The sensorless control of the machine was achieved with high-frequency voltage injection. Its core equations and possible signal processing method were presented, along with a new dynamic model making possible the tuning of the PLL-based estimator. With combination of the new dynamic model and the post-process of the FEM analysis' results, the injection-based sensorless method's limitations and also stability analysis was presented. The latter one pointed out that in case of the sensorless method's signal processing, the stator resistance is considered a sensible variable of the system. Its root cause comes from the high-frequency injection, which makes the machine impedances highly inductive.

The presented sensorless method was simulated and also measured using an experimental inverter setup developed by the authors. The simulation and measurement results coincide very well, validating the theory and the modeling. The initial angle estimation problem was solved by using stationary injection, and such combination of the injection methods was able to find the initial angle, and was able to provide angle and speed feedbacks for the control loops.

Regarding the estimator part of the system, fuzzy logic-based solutions could be an applied to handle the deviations coming from the machine parameters [27] - [28]. Another interesting approach both for the high-frequency estimation-based method and also for the drive control system a neural network-based approach. Several successful implementations of these methods on controlled electric drives are reported. [29] - [30].

The author adopted the presented control scheme to squirrel-cage induction machines and synchronous reluctance machines too, and the research results will be presented soon.

References

[1] Lin, Xiaogang, Wenxin Huang, and Wen Jiang. "Position sensorless direct torque control for pmsm based on pulse high frequency stator flux injection at low speed." 2019 IEEE 28th International Symposium on Industrial Electronics (ISIE). IEEE, 2019

[2] Medjmadj, Slimane, et al. "A salient-pole PMSM position and speed estimation at standstill and low speed by a simplified HF injection method." IECON 2017-43rd Annual Conference of the IEEE Industrial Electronics Society. IEEE, 2017

[3] Liu, J. M., and Z. Q. Zhu. "Sensorless control strategy by square-waveform high-frequency pulsating signal injection into stationary reference frame." IEEE Journal of Emerging and Selected Topics in Power Electronics 2.2 (2013): 171-180

[4] Wang, Gaolin, et al. "Sensorless control scheme of IPMSMs using HF orthogonal square-wave voltage injection into a stationary reference frame." IEEE Transactions on Power Electronics 34.3 (2018): 2573-2584

[5] Liu, J. M., and Z. Q. Zhu. "Novel sensorless control strategy with injection of high-frequency pulsating carrier signal into stationary reference frame." IEEE Transactions on Industry Applications 50.4 (2013): 2574-2583

[6] Jang, Ji-Hoon, et al. "Sensorless drive of surface-mounted permanent-magnet motor by high-frequency signal injection based on magnetic saliency." IEEE Transactions on Industry Applications 39.4 (2003): 1031-1039

[7] Kim, Sungmin, Jung-Ik Ha, and Seung-Ki Sul. "PWM switching frequency signal injection sensorless method in IPMSM." IEEE Transactions on Industry Applications 48.5 (2012): 1576-1587

[8] D. Raca, P. Garcia, D. Reigosa, F. Briz and R. Lorenz, A comparative analysis of pulsating vs. rotating vector carrier signal injection-based sensorless control, 2008 Twenty-Third Annual IEEE Applied Power Electronics Conference and Exposition, Austin, TX, 2008, pp. 879-885

[9] Jin, Xinhai, et al. "High-frequency voltage-injection methods and observer design for initial position detection of permanent magnet synchronous machines." IEEE Transactions on Power Electronics 33.9 (2017): 7971-7979

[10] Han, Bangcheng, et al. "Initial rotor position detection method of SPMSM based on new high frequency voltage injection method." IEEE Transactions on Power Electronics 34.4 (2018): 3553-3562

[11] B. Han, Y. Shi, X. Song, K. Hong and K. Mao, "Initial Rotor Position Detection Method of SPMSM Based on New High Frequency Voltage Injection Method," in IEEE Transactions on Power Electronics, Vol. 34, No. 4, pp. 3553-3562, April 2019

[12] Fu, Xinghe, et al. "Initial Rotor Position Estimation by Detecting Vibration of Permanent Magnet Synchronous Machine." IEEE Transactions on Industrial Electronics 68.8 (2020): 6595-6606

[13] S. Pekarek and P. Beccue, "Using torque-ripple-induced vibration to determine the initial rotor position of a permanent magnet synchronous machine," in IEEE Transactions on Power Electronics, Vol. 21, No. 3, pp. 818-821, May 2006

[14] Nyitrai, Attila, et al. "Multiphysics Analysis of Automotive PMaSynRM." 2019 International IEEE Conference and Workshop in Óbuda on Electrical and Power Engineering (CANDO-EPE). IEEE, 2019

[15] Szabó Gergely, Horváth Sándor, Számel László, Veszprémi Károly. "Coupled Transient Analysis of Asynchronous Machine Drives." XXXV. Jubileumi Kandó Konferencia 2019

[16] Štumberger, Gorazd, Bojan Štumberger, and Tine Marčič. "Magnetically nonlinear dynamic models of synchronous machines and experimental methods for determining their parameters." Energies 12.18 (2019): 3519

[17] B. Stumberger, G. Stumberger, D. Dolinar, A. Hamler and M. Trlep, "Evaluation of saturation and cross-magnetization effects in interior permanent-magnet synchronous motor," in IEEE Transactions on Industry Applications, Vol. 39, No. 5, pp. 1264-1271, Sept.-Oct. 2003

[18] Kim, Hyeon-Sik, et al. "Online MTPA control of IPMSM based on robust numerical optimization technique." IEEE Transactions on Industry Applications 55.4 (2019): 3736-3746

[19] W. Xu, M. M. Ismail, Y. Liu and M. R. Islam, "Parameter Optimization of Adaptive Flux-Weakening Strategy for Permanent-Magnet Synchronous Motor Drives Based on Particle Swarm Algorithm," in IEEE Transactions on Power Electronics, Vol. 34, No. 12, pp. 12128-12140, Dec. 2019

[20] Reda, A., Bouzid, A., & Vásárhelyi, J. (2020) Model predictive control for automated vehicle steering. Acta Polytechnica Hungarica, 17(7), 163-182

[21] Niu, S., Luo, Y., Fu, W., & Zhang, X. (2020) Robust model predictive control for a three-phase PMSM motor with improved control precision. IEEE Transactions on Industrial Electronics, 68(1), 838-849

[22] Zamfirache, I. A., Precup, R.-E., Roman, R. -C., & Petriu, E. M. (2022) Reinforcement Learning-based control using Q-learning and gravitational search algorithm with experimental validation on a nonlinear servo system. Information Sciences, 583, 99-120

[23] Wang, Liuping, et al. PID and predictive control of electrical drives and power converters using MATLAB/Simulink. John Wiley & Sons, 2015

[24] Kiam Heong Ang, G. Chong and Yun Li, PID control system analysis, design, and technology, IEEE Transactions on Control Systems Technology, Vol. 13, No. 4, pp. 559-576, July 2005

[25] Vukosavic, Slobodan N. Digital control of electrical drives. Springer Science & Business Media, 2007

[26] Szabó, Gergely, and Károly Veszprémi. "Sensorless Vector Control of Permanent Magnet Synchronous Machine Using High-Frequency Rotating Injection." 2021 IEEE 19th International Power Electronics and Motion Control Conference (PEMC). IEEE, 2021

[27] Precup, R. -E., Doboli, S., & Preitl, S. (2000) Stability analysis and development of a class of fuzzy control systems. Engineering Applications of Artificial Intelligence, 13(3), 237-247

[28] Roman, R. C., Precup, R. E., & Petriu, E. M. (2021) Hybrid data-driven fuzzy active disturbance rejection control for tower crane systems. European Journal of Control, 58, 373-387

[29] Chen, T., Babanin, A., Muhammad, A., Chapron, B., & Chen, C. (2020) Modified evolved bat algorithm of fuzzy optimal control for complex nonlinear systems. Rom. J. Inf. Sci. Technol., 23(T), T28-T40

[30] Ghamri, A., Boumaaraf, R., Benchouia, M. T., Mesloub, H., Goléa, A., & Goléa, N. (2020) Comparative study of ANN DTC and conventional DTC controlled PMSM motor. Mathematics and Computers in Simulation, 167, 219-230